Hindawi
International Journal of Aerospace Engineering
Volume 2019, Article ID 9457249, 12 pages
https://doi.org/10.1155/2019/9457249

Research Article

Comparative Study on Steady and Unsteady Flow in a Centrifugal Compressor Stage

Changhee Kim[1] **and Changmin Son**[2]

[1]*School of Mechanical Engineering, Pusan National University, Busan, Republic of Korea*
[2]*Department of Mechanical Engineering, Virginia Polytechnic Institute and State University, Blacksburg, VA 24061, USA*

Correspondence should be addressed to Changmin Son; changminson@vt.edu

Received 25 January 2019; Accepted 1 April 2019; Published 9 June 2019

Academic Editor: Giovanni Delibra

Steady Reynolds-averaged Navier-Stokes (RANS) simulation with the mixing-plane approach is the most common procedure to obtain the performance of a centrifugal compressor in an industrial development process. However, the accurate prediction of complicated flow fields in centrifugal compressors is the most significant challenge. Some phenomena such as the impeller-diffuser flow interaction generates the unsteadiness which can affect the steady assumption. The goal of this study is to investigate the differences between the RANS and URANS simulation results in a centrifugal compressor stage. Simulations are performed at three operating points: near surge (NS), design point (DP), and near choke (NC). The results show that the RANS simulation can predict the overall performance with reasonable accuracy. However, the differences between the RANS and URANS simulation are quite significant especially in the region that the flows are highly unsteady or nearly separated. The RANS simulation is still not very accurate to predict the time-dependent quantities of the flow structure. It shows that the URANS calculations are necessary to predict the detailed flow structures and performance. The phenomena and mechanisms of the complex and highly unsteady flow in the centrifugal compressor with a vaned diffuser are presented and analyzed in detail.

1. Introduction

Centrifugal compressors are commonly used in many industrial applications, such as the oil and gas industry and aero engines. The flow field in centrifugal compressor stages is highly complex, unsteady, three-dimensional, and turbulent. The interaction between the impeller and vaned diffuser is the source of unsteady phenomena which can affect the centrifugal compressor stage performance. The vaned diffuser suffers from the distorted upstream flow due to the jet-wake structure coming from the impeller, whereas the impeller is submitted to the potential effect of the vaned diffuser. In order to help our understanding of the flow field, it is necessary to analyze the unsteady effect in the centrifugal compressor stage.

Many research works have been undertaken numerically and experimentally to understand the impact of the unsteady flow on both stage performance and flow field. Krain [1] investigated the unsteady flow field development in the vaneless region and in the vaned diffuser of a transonic centrifugal compressor using advanced laser velocimetry. A strong wake flow was observed near the impeller exit. A highly distorted and unsteady flow was investigated in the vaned diffuser entrance region. Dean and Senoo [2] showed that the nonuniform unsteady flow at the impeller outlet is dissipated very rapidly and mixed out completely in the vaneless diffuser. Inoue and Cumpsty [3] reported that the circumferentially distorted flow from the impeller has insignificant effects on the flow in the vaned diffuser. Rodgers [4] reported experimentally that the radial gap is a crucial design parameter influencing the efficiency and pressure ratio and that an optimum radial gap exists. Shum et al. [5] found the existence of the optimum radial gap size and concluded that the unsteady impeller-diffuser interaction has an effect on impeller tip leakage flow, loss, blockage, slip, and stage pressure rise. Ibaraki et al. [6, 7] conducted the detailed flow measurements in a high-pressure ratio centrifugal compressor using laser Doppler velocimetry and particle image

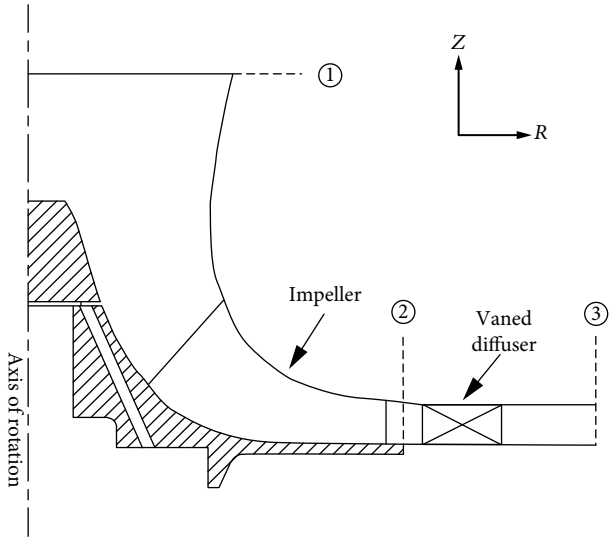

Figure 1: Cross section of the centrifugal compressor stage.

Table 1: Specifications of the centrifugal compressor stage.

Parameter	Value
Relative tip clearance, CR	2.3%
Rotating speed, N	12500 rpm
Design flow coefficient, ϕ	0.083
Design pressure ratio, Π	2.1
Impeller	
Number of blades, Z_{Imp}	11
Backsweep angle, β_2	47 deg
Inlet tip radius	70 mm
Exit tip radius	130 mm
Vaned diffuser	
Number of vanes, Z_{Diff}	10
Inlet radius	145 mm
Exit radius	165 mm

velocimetry. The interaction between the shock wave and tip leakage vortex at the inducer and flow distortion downstream of the inducer were observed. They also found that the diffuser inlet flow is influenced by the impeller flow which causes a three-dimensional distorted flow in the spanwise direction and the flow in the vaned diffuser is strongly unsteady. Ziegler et al. [8, 9] investigated the effect of the impeller-diffuser interaction on the unsteady, the time-averaged flow, and the performance in a centrifugal compressor. The results showed that in most cases smaller radial gaps introduce a more uniform flow at the diffuser vane exit and improve diffuser pressure recovery, while impeller efficiency hardly changes. The essential result of this study is that the flow structure in the diffuser can be optimized by adjusting the radial gap. Dawes [10] studied the unsteady interaction of a centrifugal impeller with its vaned diffuser using time-resolved simulation and presented that the upstream flow

Table 2: Comparison of numerical setup between the RANS and URANS simulations.

Setting	RANS (Kim et al. [17])	URANS (current work)
Turbulence model	Standard $k-\varepsilon$ turbulence model with scalable wall function	
Advection scheme	High-resolution advection scheme	
Turbulence	First-order upwind scheme	
Rotor-stator interface	Mixing-plane interface	Sliding interface
Transient scheme	—	Second-order backward Euler

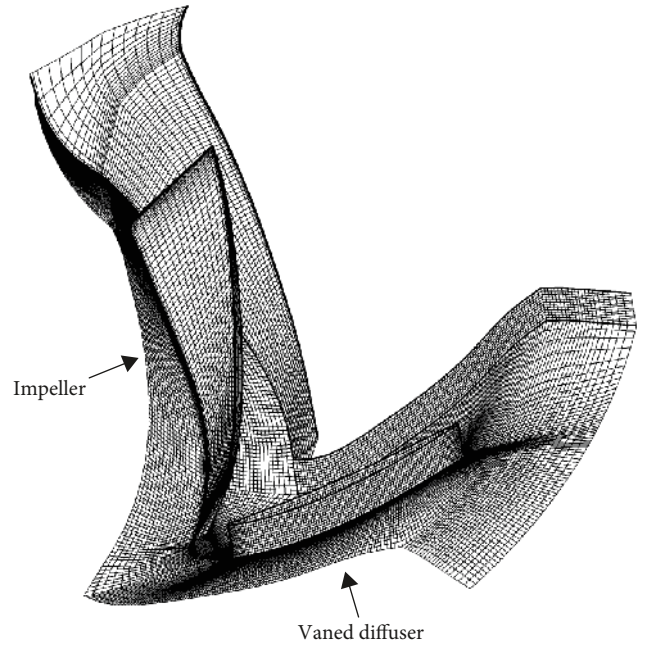

Figure 2: Computational mesh for the centrifugal compressor stage.

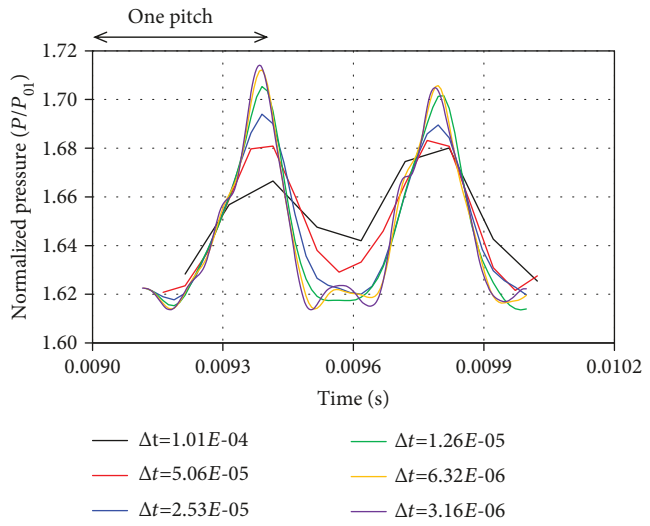

Figure 3: Solution dependency on the time step at the impeller exit.

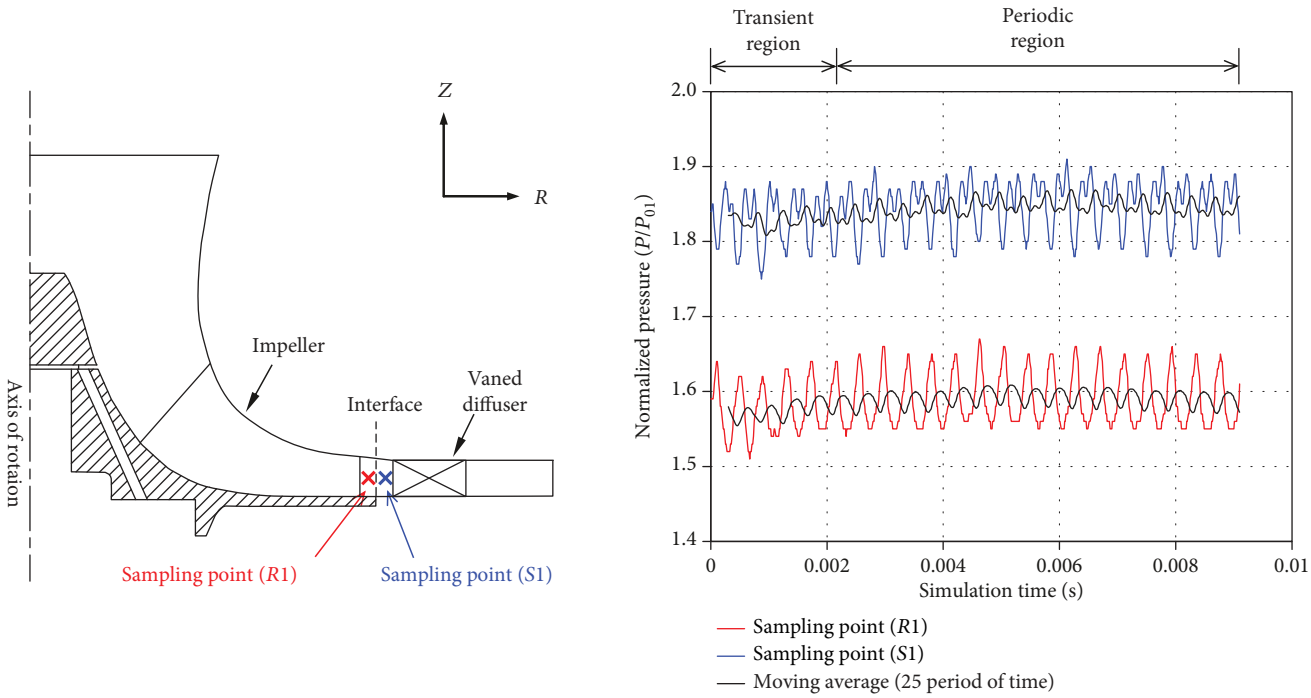

Figure 4: Static pressure at the impeller exit and vaned diffuser inlet during the calculation.

field of the vaned diffuser can affect the impeller flow field. Deniz et al. [11] examined experimentally the effect of upstream flow conditions on the performance and operating range of two different vaned diffusers. They reported that the diffuser performances are correlated with the inlet flow angle even at supersonic upstream conditions. Peeters and Sleiman [12] presented that the impeller-diffuser interaction can significantly affect the centrifugal compressor stage performance compared to the steady calculation. He et al. [13] presented that the large differences between the steady and time-averaged unsteady simulation results usually occurred at the highly unsteady or separated flow region. Trébinjac et al. [14] conducted numerical and experimental investigations in a transonic centrifugal compressor stage. The performance curve is well predicted using the unsteady simulations over the entire operating range, while the steady simulations strongly overestimate the total pressure ratio. Boncinelli et al. [15] carried out both the steady and unsteady simulations. The flow unsteadiness appeared to impact marginally the stage performance, but it has a relevant impact on the flow field. Denton [16] discussed about the loss mechanisms and effect of unsteadiness in turbomachines. Unsteady flow can affect entropy generation.

In the present paper, both steady and unsteady simulations are carried out to analyze the unsteady effects in the centrifugal compressor stage. Despite the fact that the flow in a centrifugal compressor stage is highly unsteady, the steady state assumption is still widely used by design engineers. These designers often utilize the steady predicted results as guidance in an industrial design process. Hence, the purpose of this study is to quantify the difference between the steady and unsteady calculation results for different flow rates. It is envisioned that this work would provide some useful information for the designers and when it is necessary to consider the unsteady flow effect.

2. Centrifugal Compressor Stage

The investigated model used in this work is a single-stage centrifugal compressor, which consists of a semi-inducer unshrouded impeller with 11 backswept blades and a vaned diffuser with 10 vanes. The cross-section view of the centrifugal compressor stage is shown in Figure 1. The impeller and vaned diffuser are both of the same configuration to the previous study (Kim et al. [17]). Refrigerant R134a is used as a working fluid for a centrifugal chiller. Table 1 summarizes the centrifugal compressor stage specifications. This stage has been experimentally investigated in detail by Lee [18].

3. Computational Method

The steady and unsteady simulations are carried out using the commercial computational fluid dynamics (CFD) software, ANSYS CFX 15.0, to solve the three-dimensional Reynolds-averaged Navier-Stokes (RANS) equations. Most of the solver settings are identical for the steady and unsteady simulations (Table 2). The viscous effects are modeled using the standard $k-\varepsilon$ two-equation turbulence model (Launder and Spalding [19]) with scalable wall function. A high-resolution advection scheme is selected to discretize the convective terms except turbulence, for which a first-order upwind scheme is used. The steady and unsteady simulations are conducted with single passage of the full 360° model. The computational mesh (Figure 2) is generated by ANSYS TurboGrid 15.0 software. The entire mesh consists of 1.2 M

grids and 20 elements inside the tip gap. The nondimensional wall distance, $y+$, inside the computational domain is kept between 30 and 100 on the corresponding surfaces. The current mesh and numerical setup were used and validated in the previous investigation (Kim et al. [17]). A detailed view of the mesh and comparison of steady-state performance calculations and measurements can be found in Kim et al. [17]. The same mesh is used for the steady and unsteady simulations. Total pressure and total temperature are applied as the inlet condition. The mass flow rate is adopted at the diffuser outlet. All solid wall boundaries are modeled as no-slip and adiabatic conditions. The impeller casing wall is modeled as stationary in the absolute frame of reference so that there is a relative motion between the casing wall and the impeller domain. The turbulence intensity, which was uniformly specified at the inlet, is kept as constant for all the cases with Tu = 5%. For the steady simulation, the mixing-plane approach is adopted to consider the interface between the impeller and the vaned diffuser. The conservative flow quantities at the mixing-plane interface are averaged in the circumferential direction. These mixed-out quantities are used to provide the appropriate boundary conditions for the upstream and downstream components at the mixing plane.

In the unsteady analysis, result from a steady simulation (mixing-plane interface approach) is given as an initial condition. The sliding interface approach is used to simulate the transient flow characteristics between the moving and stationary domains. Time-dependent flow behavior of unsteady simulations is determined by total time duration and time step or interval (Δt). Figure 3 shows the time step dependency of unsteady simulations at the impeller exit. The differences of unsteady pressure distributions are significant by reducing the time step size. The time step is set to $\Delta t = 6.32 \times 10^{-6}$ s, corresponding to 1 step for 0.5° rotation. The selected time step corresponds to 0.5° turning of the impeller or 65.45 steps per one pitch of the impeller blade. For each time step, all residuals are converged to $1E-05$ after 20 internal time step loops. The static pressure signals are monitored to investigate the effect of the impeller-diffuser interaction on the flow field at the impeller exit and vaned diffuser inlet during the calculations. Figure 4 presents the convergence behavior for static pressure at two monitoring points. The total simulation time is for the impeller rotating 2 revolutions. The flow field is statically stable after 0.5 revolution (transient region), and data on the last 1.5 revolution (periodic region) is used for the unsteady analysis.

4. Results and Discussion

4.1. Overall Performance. In Figure 5, the overall performance from the RANS and URANS calculations is shown with the test data. The total-to-static pressure ratio (Figure 5(a)) and polytropic efficiency (Figure 5(b)) are presented over the flow coefficient at the design speed line. It depicts the flow coefficient defined as

$$\phi = \frac{Q}{\mathrm{ND}^3}. \tag{1}$$

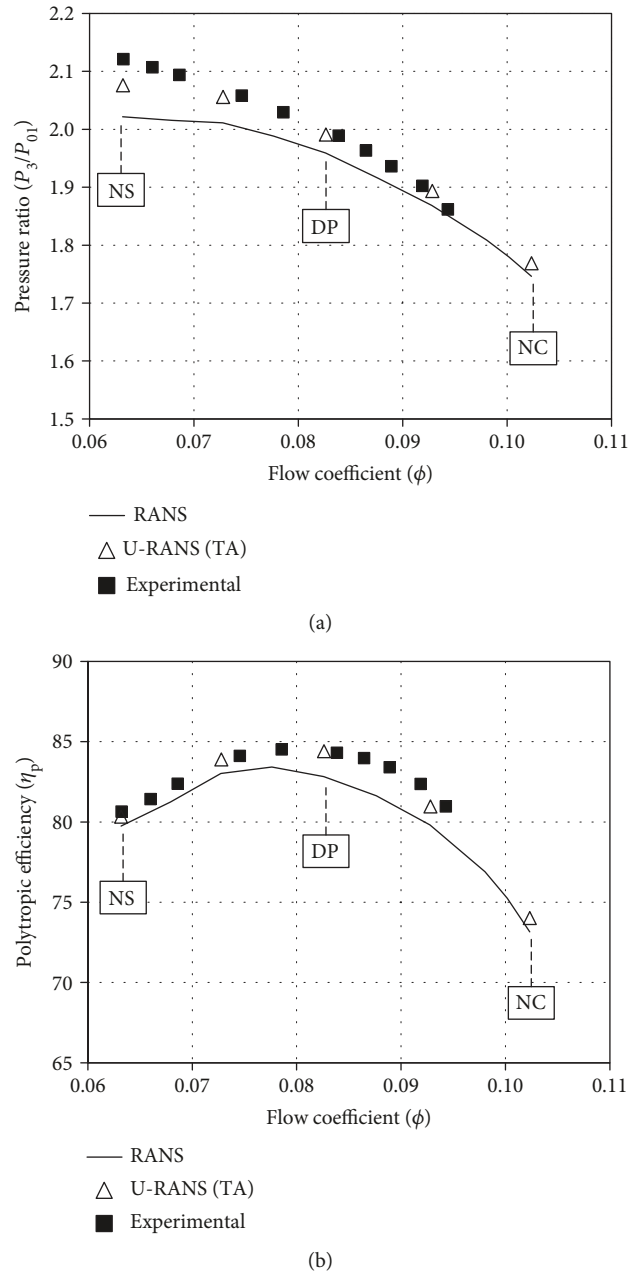

Figure 5: Compressor stage characteristics: (a) total-to-static pressure ratio and (b) polytropic efficiency.

The total-to-static pressure ratio is defined as

$$\pi = \frac{P_3}{P_{01}}. \tag{2}$$

The polytropic efficiency of the compressor stage is defined as

$$\eta_p = \frac{(H_3 - H_1) - (s_3 - s_1)(T_3 - T_1)/ln(T_3/T_1)}{(H_3 - H_1)}. \tag{3}$$

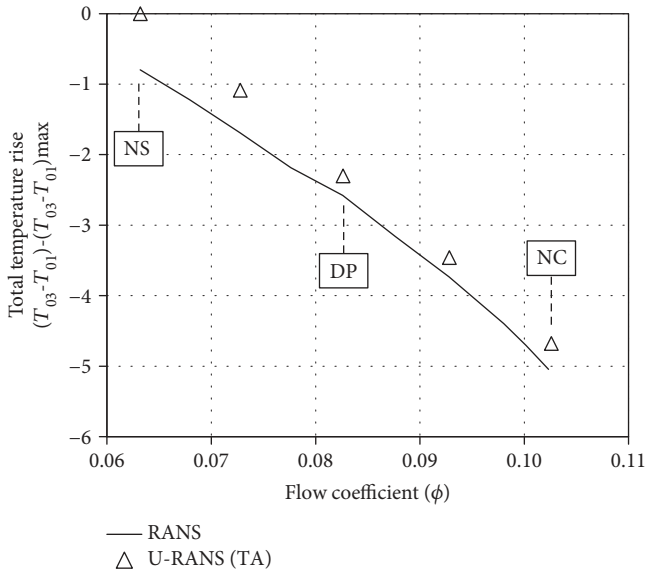

Figure 6: Total temperature rise in the compressor stage.

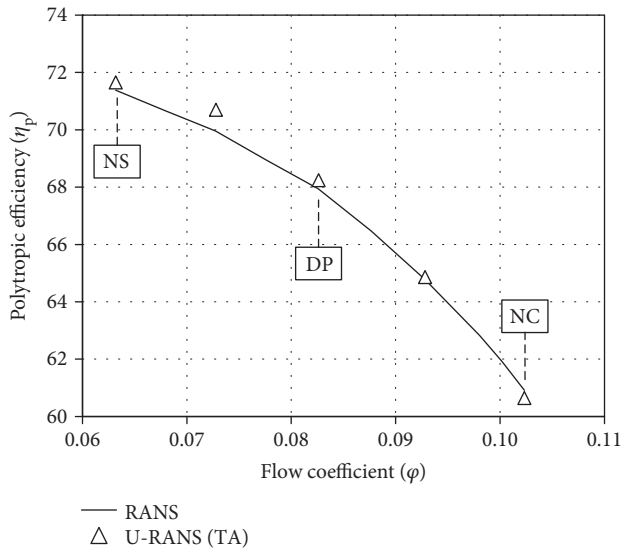

Figure 7: Polytropic efficiency in the impeller.

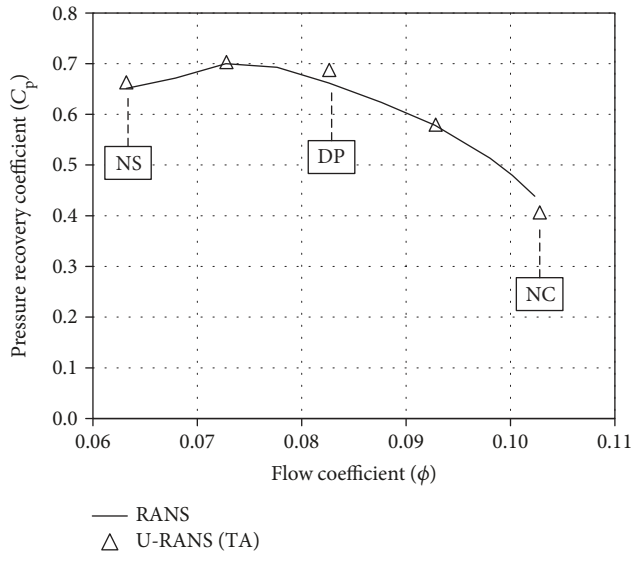

Figure 8: Static pressure recovery coefficient of the vaned diffuser.

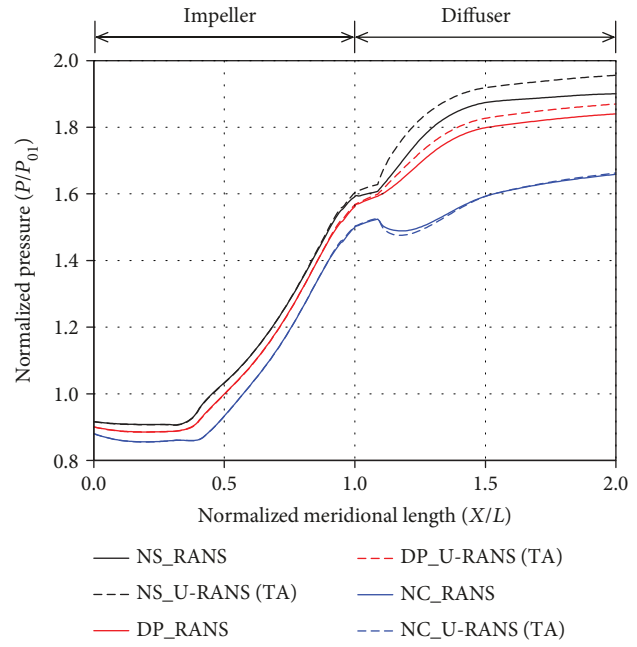

Figure 9: Normalized pressure build-up in the compressor stage.

The numerical values from the RANS and URANS simulations are obtained by mass-averaged and mass- and time-averaged values, respectively. NS, DP, and NC represent the operating conditions of near stall, design point, and near choke at the design rotating speed, respectively. The test data points are shown with the square symbol. The RANS results are shown in a solid line, and the time-averaged URANS results are marked as the triangle symbol. Both the RANS and URANS results show good agreement with the measured data. The compressor characteristic curves from the RANS calculations are slightly shifted, which leads to underestimation of the experimental results. The total-to-static pressure ratio (Figure 5(a)) at the DP is underestimated by -4.15% for the RANS and -0.4% for the URANS. At the DP, the differences of the polytropic efficiency (Figure 5(b)) are -1.96% (-1.66% points) for the RANS and -0.09% (-0.08% points) for the URANS. The difference in the polytropic efficiency at the DP is found compared the RANS with the URANS. This difference caused by the unsteadiness is 1.87% of the compressor stage loss at the DP.

Figure 6 shows the total temperature rise of the (U)RANS calculations as a function of the flow coefficient. The tendency of the total temperature rises is very similar. Therefore, the difference in the pressure ratio of the compressor stage between the RANS and URANS results seems to be pressure loss-related.

In Figures 7 and 8, the polytropic impeller efficiency and the diffuser pressure recovery coefficient are shown. From these plots, the impeller and diffuser do not show a

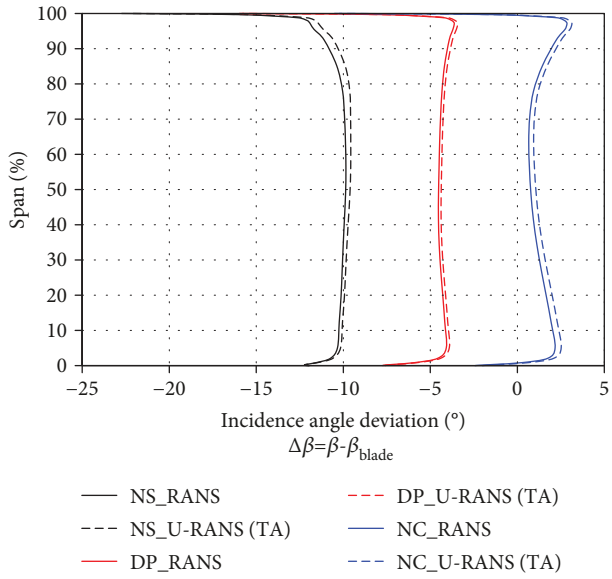

Figure 10: Incidence angle deviation distribution at the impeller inlet.

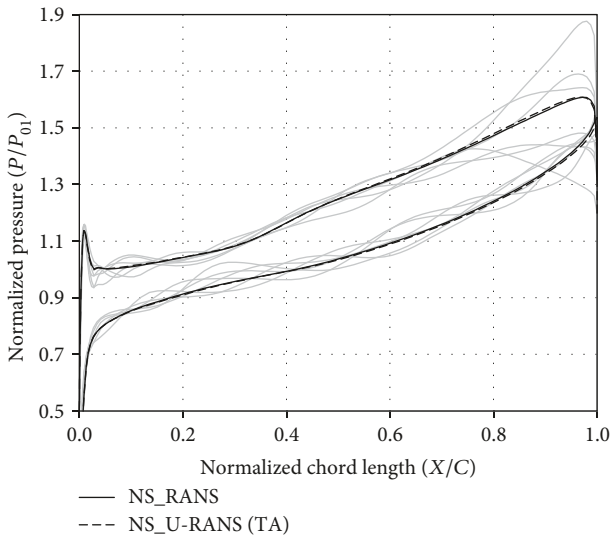

Figure 11: Blade loading on the impeller blade at 95% span for the NS.

significant difference between the RANS and URANS results over the operating range.

Figure 9 shows the normalized pressure distribution in the compressor stage at three different operating conditions. The pressure values are normalized by the inlet total pressure. The solid lines indicate the RANS simulation results. The dashed lines express the URANS simulation results. The trend of the pressure variation is quite similar in the impeller for three operating points. In addition, the pressure difference between the RANS and URANS shows in good agreement in the impeller for three operating points. This found that the centrifugal body force can be predicted exactly. The pressure distributions in the impeller are not affected by the unsteady effects except near the trailing edge region. In contrast, the pressure build-up in the

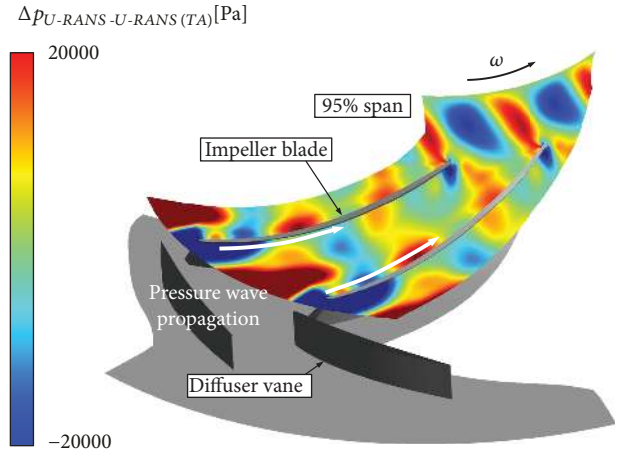

Figure 12: Unsteady potential field in the impeller for the NS at a certain point in time.

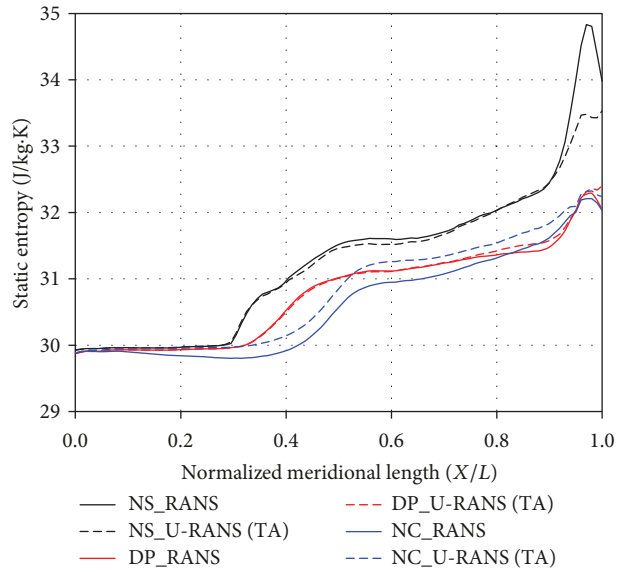

Figure 13: Static entropy distribution in the impeller.

diffuser has the discrepancies due to the unsteadiness. The discrepancies are 2.9%, 1.62%, and 0.22% at the NS, DP, and NC, respectively.

4.2. Impeller Aerodynamics. To investigate the impeller flow structure depending on the different operating points, the incidence angle deviation of the impeller is presented in Figure 10. The flow angle is the circumferential averaged value. The operating point displacement from the NC to NS leads to a decrease of the meridional velocity. At the design speed line, the mass flow reduction induces an increase in the incidence angle deviation. Also, the high incidence angle deviation occurs near the walls. The spanwise profiles for the operating points have a difference between the RANS and URANS along the blade from hub to shroud. This indicates that the flow unsteadiness affects the flow field of the inlet region.

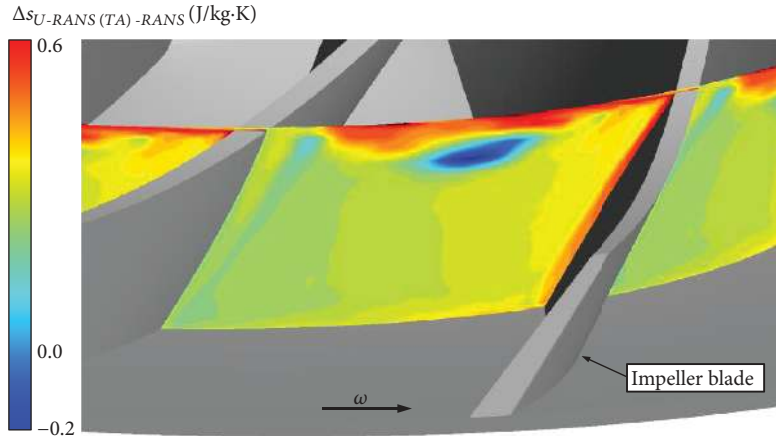

Figure 14: Entropy difference due to unsteadiness in the impeller for the NC.

Figure 11 shows the blade loading on the impeller blade at 95% span for the NS. The gray lines show the unsteady pressure distribution at six different times during one blade pitch. The RANS and URANS results show a good agreement. It shows that the time-averaged static pressure is not affected by the unsteady effects. However, the unsteady pressure distributions exhibit pressure fluctuations along the whole impeller blade. Especially, it indicates that the blade loading at the rear of the impeller is significantly affected by the impeller-diffuser interaction. The pressure fluctuations near the tip clearance can also influence on the tip leakage flow. The unsteady flow field is also the major source of a noise and/or resonance in centrifugal compressors so that an accurate prediction of an unsteady flow field is important to avoid aeromechanical difficulties.

Figure 12 shows the difference between the local static pressure and time-averaged pressure in the impeller at the 95% span for the NS. These pressure fluctuations propagate upstream along the pressure and suction side of the impeller blade.

In Figure 13, the mass-averaged static entropy distribution along the meridional length is plotted for the three operating points. There is small entropy generation in front of the impeller blade leading edge. However, a rapid increase in static entropy is observed at the impeller blade leading edge for the three operating points. This rapid change is caused by the interaction between the high velocity near the tip of the blade suction side and tip leakage flow. The location of the rapid entropy increase moves upstream with decreasing mass flow. The slope of the entropy accumulation also increases by reducing the mass flow. Towards the impeller exit, the entropy continuously increases because of the secondary flow. A similar entropy rise is observed after the trailing edge of the blade for the three operating points. This variation occurs due to the jet-wake structure and impeller-diffuser interaction. The static entropy difference between the RANS and URANS simulation results is observed in the impeller and after the blade trailing edge. In these regions, the unsteadiness of the flow makes a difference.

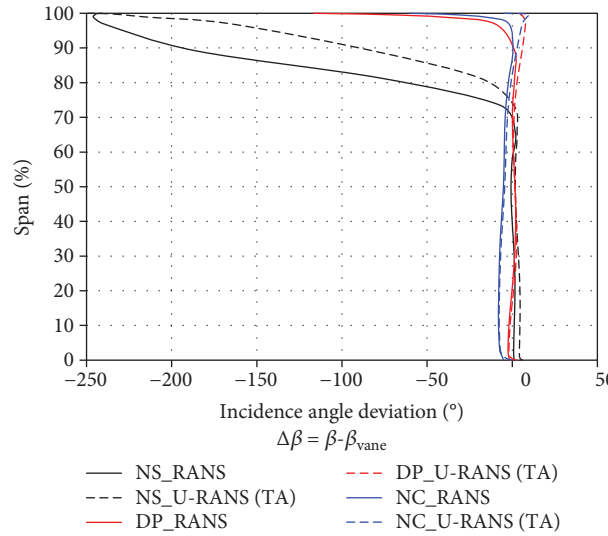

Figure 15: Incidence angle deviation distribution at the vaned diffuser inlet.

The additional entropy in the URANS simulations is generated by the unsteady effects. This is shown in Figure 14. The entropy difference between the RANS and URANS simulation results can be seen in the shroud surface and the suction side of the blade. Near the shroud region, the unsteady mixing process between the tip leakage flow and main passage flow generates the additional entropy. And it spreads in the circumferential direction by the cross flow close to the shroud. This result shows that the shroud region is the source of additional loss caused by the unsteady effects.

4.3. Diffuser Aerodynamics. A change in mass flow rate has a significant influence on the flow field behavior in the vaned diffuser. This behavior is related to the change in flow incidence angle. The radial velocity at the impeller exit decreases together with a decrease in mass flow rate. It is also observed that the tangential velocity at the impeller exit increases correspondingly. The combined effect of these causes the flow angle across the entire blade span at the impeller exit to increase.

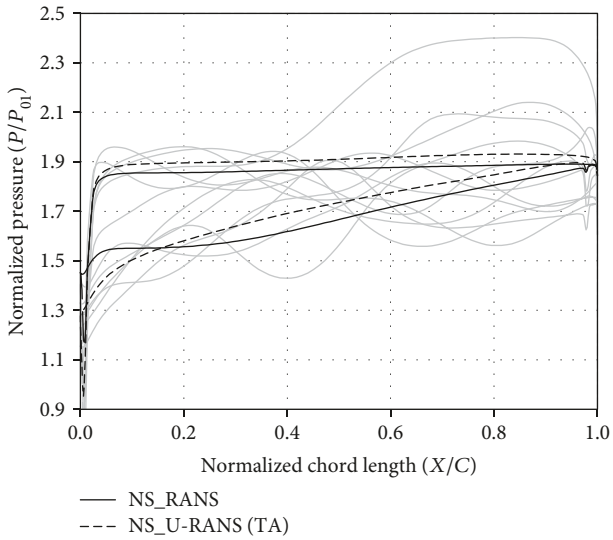

FIGURE 16: Blade loading on the diffuser vane at 95% span for the NS.

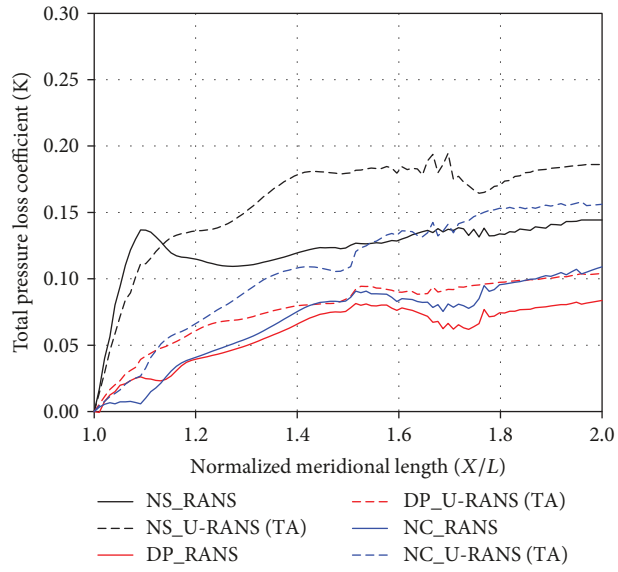

FIGURE 17: Total pressure loss coefficient distribution in the vaned diffuser.

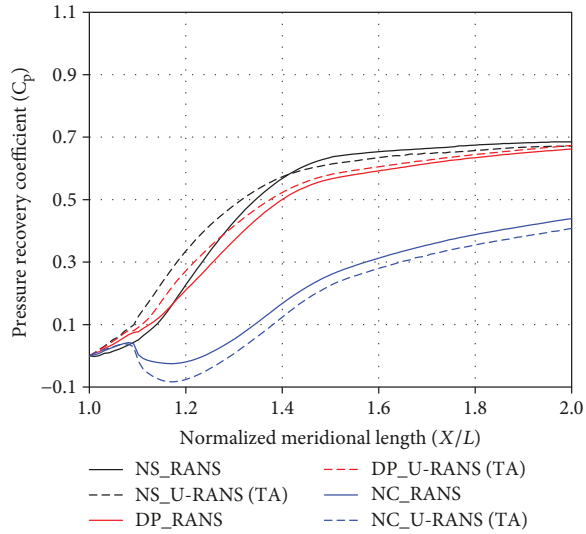

FIGURE 18: Static pressure recovery coefficient distribution in the vaned diffuser.

The impeller exit flow field is also highly distorted in the spanwise direction due to the tip leakage flow and meridional curvature. Figure 15 shows the deviation of the incidence angle at the diffuser inlet for the three operating conditions. The incidence angle is increased by the mass flow reduction. The large deviation of the incidence angle from 70% of the span to the shroud is also observed for the three operating points. This incidence angle deviation is caused by the tip leakage flow and secondary flow. The large difference of the incidence angle between the RANS and URANS is shown from 70% of the span to the shroud. This gap is affected by the unsteady effects caused by the tip leakage flow and impeller-diffuser interaction. The excessive incidence angle near the shroud generates the flow separation of the leading edge of the diffuser vane.

Figure 16 represents the blade loading on the diffuser vane at 95% span for the NS. The gray lines represent the unsteady pressure distribution at six different times during one pitch. The difference of blade loadings between the RANS and URANS simulation is observed. The unsteady pressure distributions exhibit pressure fluctuations along the whole diffuser vane. The pressure fluctuation is getting stronger towards the trailing edge of the diffuser vane. These unsteady effects are caused by the interaction between the nonuniform impeller exit flow and the diffuser vanes. The streamwise location of the unloading of the diffuser vane varies with time. These variations cause the vortex shedding in a diffuser.

As shown in Figure 8, the overall performance of the vaned diffuser does not show a significant difference due to the unsteadiness. However, Figure 16 shows a significant unsteadiness in the diffuser. To consider the local unsteady effects, the total pressure loss coefficient (Figure 17) and static pressure recovery coefficient (Figure 18) are plotted along the meridional direction.

In Figure 17, the highest losses occur in the front region of the diffuser for three operating points. In the semi-vaneless region, the flow is transonic and the boundary layer creates the losses. Downstream of the trailing edge, there is a moderate increase in loss generation. The URANS simulations in the total pressure loss coefficient overestimate the RANS simulations for the three operating points.

The static pressure recovery coefficient is shown in Figure 18. This shows a significant increase in the static pressure recovery coefficient in the front region of the diffuser for three different operating conditions. Contrary to the total pressure loss coefficient, the URANS simulations in the static pressure loss coefficient underestimate the RANS simulations for the three operating points. In the diffuser, the flow is not only affected by not only an unsteadiness but also a strong mixing.

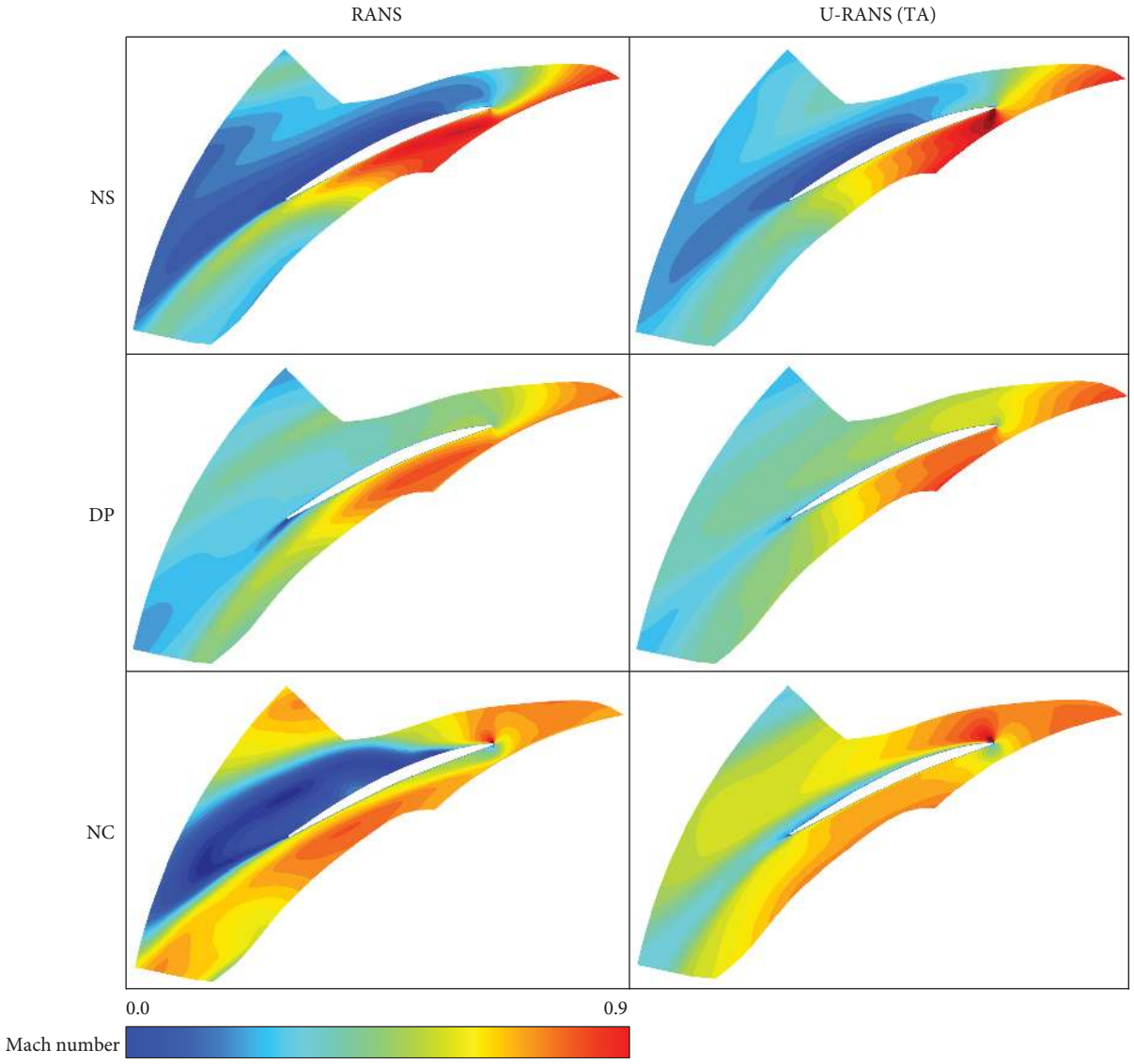

Figure 19: Mach number distribution in the vaned diffuser at the midspan.

To understand where this difference comes from, the RANS and URANS simulations at three operating points are compared. At each operating point, the Mach number distribution at midspan (Figure 19) is presented. It shows that the flow fields have a large difference. The RANS simulation results illustrate the limitations of the mixing-plane method. In the RANS results, the large separated flow region is observed near the pressure side of the diffuser vane for the NS and NC. The large separated flow region from the RANS simulations forms earlier than that from the URANS simulations for NS and NC.

Figure 20 shows the counter-rotating vortical structures in the semi-vaneless region and propagate downstream. The red zone shows the clockwise flow while the blue zone represents the counter-clockwise flow. A sequence of the transient vortical structures can be observed at the midspan of the diffuser. The wakes of the impeller blades are radially propagated and divided by the vane leading edge. The wake impinges the leading edge of the diffuser vane; it causes an increase in the incidence deviation which is related to the corner separation. The unsteady changes in the flow at the diffuser inlet have a high impact on the development of the flow behind the leading edge of the diffuser vane. When the mass flow increases, the flow becomes more radial. From the NS to NC, the vortical structures generated in the semi-vaneless region move further downstream.

5. Conclusions

A centrifugal compressor stage is investigated in detail by using the RANS and URANS simulations at the NS, DP, and NC on the design speed. This study focuses on the basic phenomena and mechanism of the complex and highly unsteady flow in the centrifugal compressor. The conclusions from this investigation are as follows:

(i) Although the RANS and URANS simulations show a very similar performance for the entire

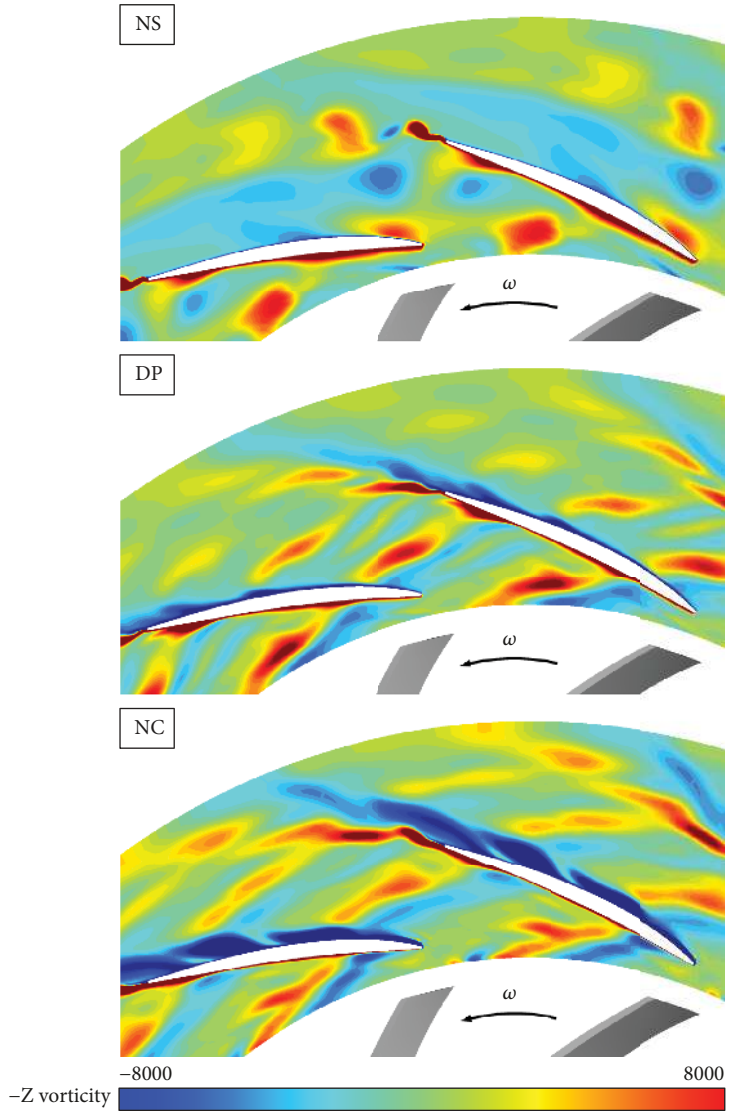

Figure 20: Vortical structures in the vaned diffuser at the midspan.

compressor stage, the flow structures developed in the vaned diffuser are significantly different. This difference of the flow field in the vaned diffuser is a consequence of the mixing-plane approach, where the flow field is averaged out circumferentially at the interface

(ii) The flow field in the compressor stage is highly unsteady due to the strong impeller-diffuser interaction

(iii) The unsteady pressure distributions caused by the impeller-diffuser interaction exhibit pressure fluctuations along the whole impeller blade and diffuser vane. These pressure fluctuations propagate upstream and downstream. The impeller-diffuser interaction has large influence on the blade and vane loading

(iv) The entropy difference between the RANS and URANS simulation can be seen in the shroud surface and the suction side of the blade. Near the shroud region, the unsteady mixing process between the tip leakage flow and main passage flow generates the additional entropy

(v) The vaned diffuser experiences strong flow variations with the transonic flow and the jet-wake flow

(vi) The highest losses are observed in the semi-vaneless space for three operating points

(vii) In the diffuser, the flow is not only affected by not only an unsteadiness but also a strong mixing

Nomenclature

Latin

RANS: Reynolds-averaged Navier-Stokes
URANS: Unsteady Reynolds-averaged Navier-Stokes

URANS (TA): Time-averaged URANS
NS: Near surge
DP: Design point
NC: Near choke
CFD: Computational fluid dynamics
CR: Relative tip clearance, $t/(t + b_2)$
t: Tip clearance (mm) or time (s)
b: Impeller blade height (mm)
N: Rotating speed (rpm)
Z: Number of blades or vanes
FFT: Fast Fourier transformation
y+: Dimensionless wall distance
Q: Volume flow rate (m^3/s)
D: Impeller diameter (m)
H: Static enthalpy (J/kg)
s: Static entropy (J/kg·K)
P: Pressure (Pa)
T: Temperature (K)
Tu: Turbulence intensity (%)
C_p: Static pressure recovery coefficient $(P - P_2)/(P_{02} - P_2)$
K: Total pressure loss coefficient $(P_{02} - P_0)/(P_{02} - P_2)$

Greek

β: Blade flow angle (deg)
ϕ: Flow coefficient
π: Pressure ratio
η_p: Polytropic efficiency

Subscripts

0: Stagnation condition
1: Impeller inlet
2: Impeller exit
3: Diffuser exit
Imp: Impeller
Diff: Diffuser.

Data Availability

The data used to support the findings of this study are included within the article.

Conflicts of Interest

The authors declare that they have no conflicts of interest.

Acknowledgments

We would like to thank LG Electronics, which supported this research. This work was partly supported by the Human Resources Development program (No. 20184030202060) of the Korea Institute of Energy Technology Evaluation and Planning (KETEP) grant funded by the Korea government Ministry of Trade, Industry and Energy (MOTIE). This work was also partly supported by the Korea Institute of Energy Technology Evaluation and Planning (KETEP) and the Ministry of Trade, Industry and Energy (MOTIE) of the Republic of Korea (No. 20181110100400).

References

[1] H. Krain, "A study on centrifugal impeller and diffuser flow," *Journal of Engineering for Power*, vol. 103, no. 4, pp. 688–697, 1981.

[2] R. C. Dean and Y. Senoo, "Rotating wakes in vaneless diffusers," *Journal of Basic Engineering*, vol. 82, no. 3, pp. 563–570, 1960.

[3] M. Inoue and N. A. Cumpsty, "Experimental study of centrifugal impeller discharge flow in vaneless and vaned diffusers," *Journal of Engineering for Gas Turbines and Power*, vol. 106, no. 2, p. 455, 1984.

[4] C. Rodgers, "The performance of centrifugal compressor channel diffusers," in *ASME 1982 International Gas Turbine Conference and Exhibit*, pp. 1–13, London, England, April 1982.

[5] Y. K. P. Shum, C. S. Tan, and N. A. Cumpsty, "Impeller-diffuser interaction in a centrifugal compressor," *Journal of Turbomachinery*, vol. 122, no. 4, pp. 777–786, 2000.

[6] S. Ibaraki, T. Matsuo, H. Kuma, K. Sumida, and T. Suita, "Aerodynamics of a transonic centrifugal compressor impeller," *Journal of Turbomachinery*, vol. 125, no. 2, pp. 346–351, 2003.

[7] S. Ibaraki, T. Matsuo, and T. Yokoyama, "Investigation of unsteady flow field in a vaned diffuser of a transonic centrifugal compressor," *Journal of Turbomachinery*, vol. 129, no. 4, pp. 686–693, 2007.

[8] K. U. Ziegler, H. E. Gallus, and R. Niehuis, "A study on impeller-diffuser interaction—part I: influence on the performance," *Journal of Turbomachinery*, vol. 125, no. 1, pp. 173–182, 2003.

[9] K. U. Ziegler, H. E. Gallus, and R. Neihuis, "A study on impeller-diffuser interaction – part 2: detailed flow analysis," *Journal of Turbomachinery*, vol. 125, no. 1, pp. 183–192, 2003.

[10] W. N. Dawes, "A simulation of the unsteady interaction of a centrifugal impeller with its vaned diffuser: flow analysis," *Journal of Turbomachinery*, vol. 117, no. 2, pp. 213–222, 1995.

[11] S. Deniz, E. M. Greitzer, and N. A. Cumpsty, "Effects of inlet flow field conditions on the performance of centrifugal compressor diffusers: part 2 – straight-channel diffuser," *Journal of Turbomachinery*, vol. 122, no. 1, pp. 11–21, 2000.

[12] M. Peeters and M. Sleiman, "A numerical investigation of the unsteady flow in centrifugal stages," *ASME Turbo Expo 2000: Power for Land, Sea, and Air*, 2000, pp. 1–8, Munich, Germany, May 2000.

[13] N. He, A. Tourlidakis, and R. L. Elder, "Comparisons of steady and time-averaged unsteady flow predictions for impeller-diffuser interactions in a centrifugal compressor stage," *ASME Turbo Expo 2007: Power for Land, Sea, and Air*, 2007, pp. 1129–1140, Montreal, Canada, May 2007.

[14] I. Trébinjac, P. Kulisa, N. Bulot, and N. Rochuon, "Effect of unsteadiness on the performance of a transonic centrifugal compressor stage," *Journal of Turbomachinery*, vol. 131, no. 4, article 041011, 2009.

[15] P. Boncinelli, M. Ermini, S. Bartolacci, and A. Arnone, "Impeller-diffuser interaction in centrifugal compressors: numerical analysis of Radiver test case," *Journal of Propulsion and Power*, vol. 23, no. 6, pp. 1304–1312, 2007.

[16] J. D. Denton, "The 1993 IGTI scholar lecture: loss mechanisms in turbomachines," *Journal of Turbomachinery*, vol. 115, no. 4, pp. 621–656, 1993.

[17] C. Kim, H. Lee, J. Yang, C. Son, and Y. Hwang, "Study on the performance of a centrifugal compressor considering running tip clearance," *International Journal of Refrigeration*, vol. 65, pp. 92–102, 2016.

[18] H. Lee, *Assessment of Impeller Performance Characteristic considering Working Environment of a Centrifugal Compressor, [Ph.D. Thesis]*, Pusan National University, Busan, Republic of Korea, 2016.

[19] B. E. Launder and D. B. Spalding, "The numerical computation of turbulent flows," *Computer Methods in Applied Mechanics and Engineering*, vol. 3, no. 2, pp. 269–289, 1974.